

Single-shot sorting of Mössbauer time-domain data at X-ray free electron lasers

Miriam Gerharz,¹ Willi Hippeler,^{2,3} Berit Marx-Glowna,^{2,3} Sakshath Sadashivaiah,^{2,3} Kai S. Schulze,⁴ Ingo Uschmann,⁴ Robert Lötzsch,⁴ Kai Schlage,⁵ Sven Velten,^{5,6} Dominik Lentrodt,⁷ Lukas Wolff,¹ Olaf Leupold,⁵ Ilya Sergeev,⁵ Hans-Christian Wille,⁵ Cornelius Strohm,⁵ Marc Guetg,⁵ Shan Liu,⁵ Gianluca Aldo Geloni,⁸ Ulrike Boesenberg,⁸ Jörg Hallmann,⁸ Alexey Zozulya,⁸ Jan-Etienne Pudell,⁸ Angel Rodriguez-Fernandez,⁸ Mohamed Youssef,⁸ Anders Madsen,⁸ Lars Bocklage,^{5,6} Gerhard G. Paulus,⁴ Christoph H. Keitel,¹ Thomas Pfeifer,¹ Ralf Röhlsberger,^{2,3,4,5,6} and Jörg Evers^{*1}

¹Max Planck Institute for Nuclear Physics, 69117 Heidelberg, Germany

²Helmholtz Institute Jena, 07743 Jena, Germany

³GSI Helmholtzzentrum für Schwerionenforschung, 64291 Darmstadt, Germany

⁴Friedrich-Schiller-Universität Jena, 07743 Jena, Germany

⁵Deutsches Elektronen-Synchrotron DESY, 22607 Hamburg, Germany

⁶The Hamburg Centre for Ultrafast Imaging CUI, 22761 Hamburg, Germany

⁷Albert-Ludwigs University of Freiburg, 79104 Freiburg, Germany

⁸European X-Ray Free-Electron Laser Facility, 22869 Schenefeld, Germany

Mössbauer spectroscopy is widely used to study structure and dynamics of matter with remarkably high energy resolution, provided by the narrow nuclear resonance line widths. However, the narrow width implies low count rates, such that experiments commonly average over extended measurement times or many x-ray pulses (“shots”). This averaging impedes the study of non-equilibrium phenomena. It has been suggested that X-ray free-electron lasers (XFELs) could enable Mössbauer single-shot measurements without averaging, and a proof-of-principle demonstration has been reported. However, so far, only a tiny fraction of all shots resulted in signal-photon numbers which are sufficiently high for a single-shot analysis. Here, we demonstrate coherent nuclear-forward-scattering of self-seeded XFEL radiation, with up to 900 signal-photons per shot. We develop a sorting approach which allows us to include all data on a single-shot level, independent of the signal content of the individual shots. It utilizes the presence of different dynamics classes, i.e. different nuclear evolutions after each excitation. Each shot is assigned to one of the classes, which can then be analyzed separately. Our approach determines the classes from the data without requiring theory modeling nor prior knowledge on the dynamics, making it also applicable to unknown phenomena. We envision that our approach opens up new grounds for Mössbauer science, enabling the study of out-of-equilibrium transient dynamics of the nuclei or their environment.

The exceptional resolution of Mössbauer spectroscopy results from the narrow linewidth of the nuclei and the recoilless interaction of photons in condensed matter due to the Mössbauer effect [1]. It forms the basis for their widespread application relying on high energy resolution [2]. In the traditional setup, radioactive sources are used to record spectra over extended measurement times [3]. Synchrotron radiation sources can considerably speed up the measurement and allow for measurements in the time domain [4, 5], but the narrow spectral width nevertheless implies the need for averaging over many x-ray shots. The reason is that the signal rate per shot is low since the spectral width of the x-ray light is orders of magnitude broader than the nuclear resonance, such that the vast majority of the intense initial x-ray light is off-resonant and hence not contributing to the excitation.

This averaging requirement poses a severe challenge for studying statistical or non-repetitive dynamics, out-of-equilibrium dynamics or related phenomena with Mössbauer spectroscopy [6]. If the sample dynamics is not always the same after each x-ray shot, then the averaging inevitably ranges over different evolution pathways from the out-of-equilibrium state back into equilibrium, thereby impeding their disentangling and understanding.

For instance, statistical nuclear dynamics are expected

in the random sequence of coherent and incoherent emissions from a higher-excited nuclear ensemble, potentially involving the transient formation of entanglement [7–9]. More generally, Mössbauer nuclei are widely used to probe the dynamics of their surrounding host material [3, 4, 10], with even non-repetitive host dynamics being mapped onto the nuclear dynamics. Particularly following external stimuli [11–16] the nuclear dynamics can change drastically. In the simplest case, the stimulus induces dynamics only with a certain success probability. More interestingly, the host dynamics can involve quantum mechanical superpositions, probabilistically leading to different measurement outcomes. Examples include the laser pumping of the electronic sub-system of the host [13], which can also be prepared in a superposition state. Laser-pumping can also control the vibrational state of the host [14], or the switching of spin-crossover complexes [15, 17]. Analogously, magnons have been studied via their transient impact on the nuclear dynamics [16]. In chemistry [3], Mössbauer spectroscopy is pivotal, e.g., for studying biochemical reactions involving iron [18], but the study of short-lived transient intermediate states is difficult using Mössbauer spectroscopy [19].

Here, we demonstrate the disentangling of different Mössbauer dynamics by analyzing time-domain data on

the single-shot level. For this, we tackle the averaging challenge from two sides. First, we demonstrate coherent nuclear forward scattering of self-seeded radiation delivered by the European XFEL [20, 21], which allowed us to record Mössbauer datasets with up to 900 signal photons per x-ray shot using the isotope ^{57}Fe . These shots with highest photon number directly reveal the nuclear dynamics up to about 50 ns after excitation. Second, we develop an approach which generalizes the analysis to shots with lower signal photon rate, and to longer times after excitation. It relies on the presence of distinct evolution pathways from out-of-equilibrium back into equilibrium, which we denote as dynamics classes. We determine the classes from the data, and assign each shot to a class. Analyzing the shots of each class separately then avoids an averaging over different dynamics. The purely data-driven approach does not involve theoretical modeling, such that it applies to a priori unknown effects.

Increasing the signal photon rate until sufficient time-domain data can be recorded using single x-ray shots [6] is a seemingly simple solution to the averaging challenge. XFELs [20, 22–24] are routinely used for single-shot measurements involving electronic resonances [25–27] and have recently moved this approach also within reach for Mössbauer resonances. As a first proof-of-principle experiment, Chumakov and co-workers extracted the nuclear hyperfine splitting in ^{57}Fe from single-shot data with about 60 signal photons [28]. Meanwhile, self-seeding enabled a further increase in the resonant x-ray flux [21, 29–31]. This way, recently the ultra-narrow Mössbauer transition in ^{45}Sc could resonantly be excited [32]. However, the corresponding observation of coherent nuclear forward scattering, which is the key requirement for most applications of Mössbauer nuclei, has not been reported before.

Despite this progress, recording Mössbauer single-shot datasets beyond the proof-of-principle stage remains a challenge, since due to the XFEL photon-number distribution [33] the shots with highest signal-photon number only form a negligible fraction of all shots [28]. The vast majority of shots typically does not have sufficient signal for a single-shot analysis. Increasing the x-ray intensity further is subject to sample damage, since the “probe-before-destroy” paradigm [34] established for electronic scattering cannot straightforwardly be generalized to Mössbauer nuclei due to the long lifetimes of the nuclear excited states. This is particularly important if focusing to smaller excitation volumes is desired in order to avoid extensive spatial averaging. Recording Mössbauer single-shot data is further limited by the dynamical range of the commonly-used avalanche photodiode (APD) detectors, since the overall exponential decay of the scattered photon intensity typically spans over several orders of magnitude, thereby exceeding the linear detection range. As an example, in the present experiment, we observe APD saturation effects at early times in the shots with highest signal-photon number, even though they resolve the nuclear dynamics only for about

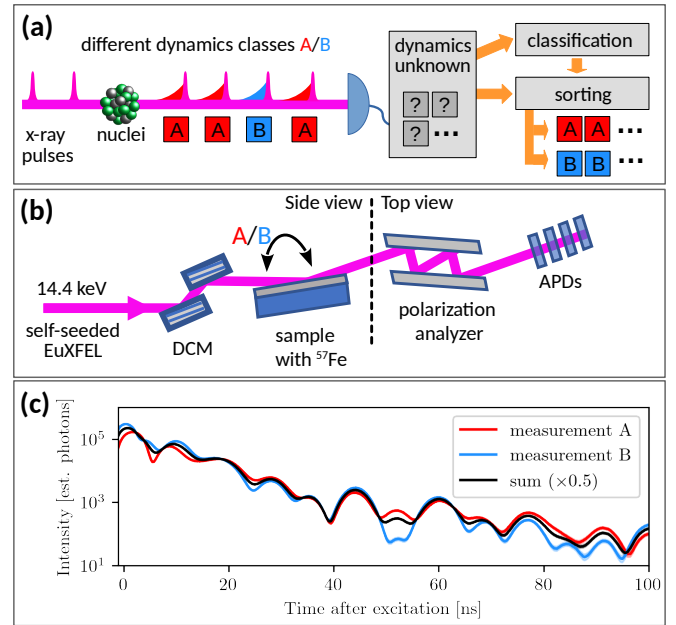


FIG. 1. (a) Single-shot sorting. We consider a generic experiment in which Mössbauer nuclei may undergo different dynamics following an x-ray excitation. Two dynamics classes “A” and “B” are indicated in red and blue as examples. The information on the dynamics is typically lost for most shots during the measurement (gray squares). Our data-driven approach identifies different dynamics classes, and subsequently sorts all shots according to the identified classes. This way, the classes can be analyzed separately, avoiding an averaging over different dynamics. (b) Schematic experimental setup at European XFEL. The self-seeded x-rays pass through a double-crystal monochromator (DCM), which removes the SASE background, and are then reflected from a thin-film waveguide containing ^{57}Fe nuclei. The nuclear-resonant signal and the off-resonant background are separated using a polarization analyzer. The time-dependent intensity of the x-rays scattered by the nuclei is then recorded using avalanche photo diodes (APD). The two dynamics classes are deterministically implemented using slightly different scattering geometries, as explained in the main text. (c) Average intensities as a function of time after x-ray excitation for dynamics classes A (red) and B (blue) separately, as well as their average (black). Only the latter signal is accessible without per-shot information on the dynamics. The shaded areas around the lines indicate the 1σ uncertainty band (see Appendix A).

50 ns after excitation. Another challenge is the desired scope of single-shot measurements, which is to probe non-repetitive phenomena. In [28], a known theory was fitted to the data in order to extract a single parameter, namely the frequency of an oscillation throughout the entire time-domain. By contrast, lifting the requirement to average over many shots is particularly important if the phenomenon under study has a comparably subtle effect on the time-domain data. Further, the requirement of fitting theory models restricts the analysis to known effects.

We overcome these challenges in directly recording and

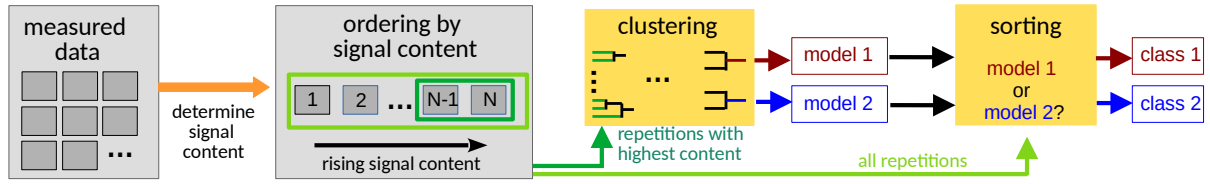


FIG. 2. Overview of the clustering and sorting. A subset of shots with highest signal content is used to identify different dynamics classes using a clustering algorithm. The resulting two models are then used as a reference in order to sort all shots of the experiment into corresponding sets which can then be analyzed separately.

evaluating Mössbauer single-shot datasets using a sorting approach on the single-shot level. Note that sorting approaches are well-established, e.g., in the context of coherent diffractive imaging [35–38], where the scattering data is used to determine the sample orientation on a per-shot basis. However, this classification is concerned with geometric properties, and not with dynamics. Another example is coherent correlation imaging [39], which classifies recorded camera images in Fourier space. Measure-and-sort approaches are also used involving auxiliary diagnostics measurements, e.g., to determine the unknown delay between optical pump and XFEL probe pulses [40], or to characterize XFEL pulses temporally [41, 42] and spectrally [43]. However, analogous approaches have not been explored with nuclear resonances before, and standard XFEL diagnostics does not straightforwardly apply to nuclear resonances because of their ultra-narrow spectral width, which typically cannot be resolved.

The schematic setup of our approach is illustrated in Fig. 1(a). We consider a generic Mössbauer experiment at an XFEL source (Fig. 1(a)) comprising a large number of shots, each initiated by the arrival of an x-ray pulse. After each x-ray excitation, detectors record the time-dependent scattered light intensity as a signature of the nuclear dynamics. As an example, one of two dynamics classes (A or B) is randomly realized in each shot. For most shots, the information on the dynamics class is not accessible by standard measurement approaches due to insufficient signal photon statistics, as indicated by the gray squares. Our goal therefore is to sort the data on a single-shot level such that the dynamics classes can be distinguished and analyzed separately.

In order to demonstrate our approach, we performed an experiment at the Materials Imaging and Diagnostics (MID) instrument of the European X-ray Free Electron Laser [44]. The schematic setup is shown in Fig. 1(b). The XFEL was operated in self-seeding mode [21] with an average pulse energy of $170\text{ }\mu\text{J}$ and bandwidth of 1.2 eV . The accelerator was operated in the 2.2 MHz mode, with 30 pulses per train and 440 ns separation between two subsequent pulses, which matches the nuclear life time very well. The photon energy was set to the nuclear resonance energy of 14.4 keV employing absolute energy measurements via the Bond method [45]. The incoming self-seeded x-rays pass MID's Si(111) double-crystal monochromator (DCM) with about 1 eV trans-

mission bandwidth, in order to remove the off-resonant SASE background. The x-rays are naturally polarized in the horizontal plane, and a channel-cut Si(840) polarization analyzer in crossed setting is used to block this polarization channel, thereby protecting the avalanche photo-diode detectors from the incident beam. The ^{57}Fe Mössbauer nuclei are embedded in a thin-film waveguide sample (see Appendix D) aligned to reflect the beam in grazing incidence geometry. A weak external magnetic field is applied to align the nuclear magnetization along the beam propagation direction, so that the circular polarizations are eigen-polarizations and the incident horizontal linear σ -polarization experiences strong scattering into the perpendicular π -polarization. This polarization component will pass the analyzer and its time-dependent intensity is recorded with APDs. An averaged detection signal is shown in Fig. 1. Example single shot raw data with high, medium and low signal content are shown in the Supplemental Figs. S1 and S2 (see Appendix B).

To allow for a quantitative assessment of our approach, we designed the experiment such that it features two different dynamics classes, and that it is known which shot belongs to which class. To this end, two separate measurements are performed using a single target, but for two slightly different incident angles of the x-rays onto the waveguide, which represent the two dynamics classes (indicated as A/B in Fig. 1(b); see Appendix D). This way, the time-domain data of each of the two classes can be obtained separately by averaging over the data of each measurement for later reference. This information is blinded in the actual analysis. The two measured reference datasets averaged over all shots of each subset are shown in Fig. 1(c). They can be well-described by standard low-excitation theory (see Appendix D), and exhibit characteristic differences at around 5 ns after excitation, around 50 ns , and after 70 ns . Note that the measured data are not histograms of signal photon arrival times, as they are established, e.g., for nuclear resonant scattering experiments at synchrotrons. Rather, they are sums of the full APD detector signals, since a disentangling of shots with tens or even hundreds of signal photons into individual arrival times is challenging (see Supplemental Fig. S1).

For the analysis, we do not use any of the prior knowledge about the measurement geometry throughout the analysis. Instead, the information on the dynamics class

is eliminated by combining the different shots of the two measurements into a single dataset, with its average shown as the black line in Fig. 1(c). The analysis sequence is illustrated in Fig. 2. The first step is to identify dynamics classes (model 1 and 2) in the “blinded” data (indicated by the gray rectangles), which can then be used to sort all shots accordingly. For this clustering step, only a selection of the shots with the highest signal content is used, which circumvents the statistical uncertainty in the data associated with low-count shots. This way time-domain data representing the specific features of each class can be extracted more reliably from the measured data. In the following we denote this step as model-building. Generally, Mössbauer time-domain data features an approximately exponentially decaying scattered light intensity, due to the spontaneous emission of the nuclei. Shots suitable for the model-building should ideally contain information, i.e., recorded signal photons, across a broad time range after excitation, which is why the logarithm of the APD trace is applied to linearize this scaling. The signal content is then defined as sum over the logarithm of the APD trace (see Appendix C). To avoid prompt artifacts from the intense incident x-ray pulse, the first 3 ns are excluded from the analysis (see Appendix B).

In order to search for the presence of different dynamics classes, we employ an agglomerative clustering algorithm [46] on the set of the N_{hs} shots with highest signal content. The clustering is based on calculating the pairwise distances between the N_{hs} shots. As a distance measure $d(a, b)$ between two shots a and b , we use the negative Poissonian log-likelihood $P(a, b) = -\sum_i a_i \cdot \ln b_i - b_i - \ln \Gamma(a_i + 1)$, symmetrized by using the maximum of both directions $d(a, b) = \max[P(a, b), P(b, a)]$ and evaluated within an analysis region of interest (ROI) on the time axis. As illustrated in the “clustering” box in Fig. 2, the two closest shots are joined into a single cluster. This clustering step is then repeated until only two clusters remain (For the result when enforcing three clusters see Ext. Data Fig. S6 and Appendix F). We employ the complete-linkage measure [47] to quantify the distance between two clusters, which is defined by the maximum of the pairwise distances between individual elements of the two clusters.

Next, we assess if the data indeed comprises different dynamics classes, by evaluating the quality and consistency of the clustering. For this, we use the silhouette score [48], which quantifies how similar a shot is to the other elements of its own cluster, on a scale given by its distance to the other clusters. The measure compares the distance \bar{d}_i of shot i to the averaged time-domain data of its own cluster normalized by its standard deviation, with the respective distance \bar{d}'_i to the second cluster. The silhouette score of a cluster then is evaluated as $s_i = (\bar{d}_i - \bar{d}'_i)/\max\{\bar{d}_i, \bar{d}'_i\}$, and thus ranges from -1 to $+1$. A high score requires that the distance of shot i to its own cluster is much smaller than the distances to the shots of the other clusters, $\bar{d}_i \gg \bar{d}'_i$. Therefore, a

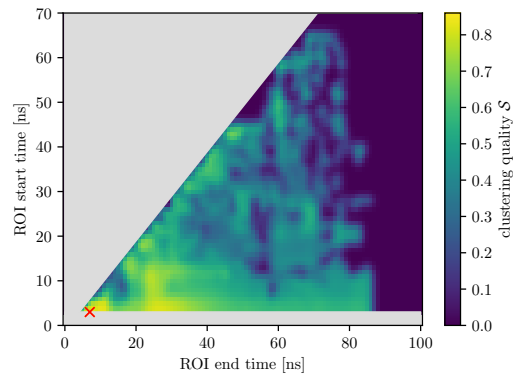


FIG. 3. Overall clustering quality \mathcal{S} as function of the analysis region of interest start and end times. Results are shown for the subset of $N_{hs} = 20$ shots with highest signal content. A moving Gaussian average filter of width $\sigma = 1\text{ ns}$ was applied to the data to reduce the influence of outliers and to favor stable analysis parameter regions. The lighter the color, the better the clustering quality \mathcal{S} , with the optimum found for the analysis ROI of (3 ns, 7 ns) and marked by the red cross. In gray invalid regions are marked.

high mean silhouette score \bar{s}_j averaged over all elements in cluster j indicates that indeed a separate dynamics class was successfully identified in the data. As a measure for the overall clustering quality \mathcal{S} of both clusters, we use the minimum of the average scores of the two clusters $\mathcal{S} = \min_{j \in \text{clusters}} \{\bar{s}_j\}$ to ensure that both dynamics classes are well-represented. This clustering quality measure can be simply extended to more clusters and can be used to identify the optimal number of clusters, which in our case results in two clusters as expected.

In order to determine the optimum analysis parameters, i.e., the number of highest-signal shots N_{hs} and the analysis ROI, we maximize the clustering quality \mathcal{S} . For this, the above analysis is systematically repeated for different numbers of shots N_{hs} and analysis ROIs. This way, the analysis parameters for the model building are fixed based on the experimental data without the need for prior knowledge about the system, nor theory modeling of it. As an example, we show the overall clustering quality \mathcal{S} as function of start- and end time of the analysis ROI for $N_{hs} = 20$ shots in Fig. 3. In order to reduce the influence of outliers and to favor stable analysis parameter regions, a narrow moving Gaussian average filter of width $\sigma = 1\text{ ns}$ is applied to the clustering quality \mathcal{S} in this figure. We find that best clustering qualities are grouped in certain ROI ranges, and we select the optimum ROI via the maximum of the clustering quality, indicated by the red cross in Fig. 3. Early times for the ROI are likely favored since the signal rate rapidly drops with time after excitation due to the exponential decay. We found that the clustering quality \mathcal{S} is maximized by including the $N_{hs} = 20$ shots with highest signal content out of all 362,610 shots into the model building, and by using an analysis ROI between 3 ns and 7 ns. Note that the clus-

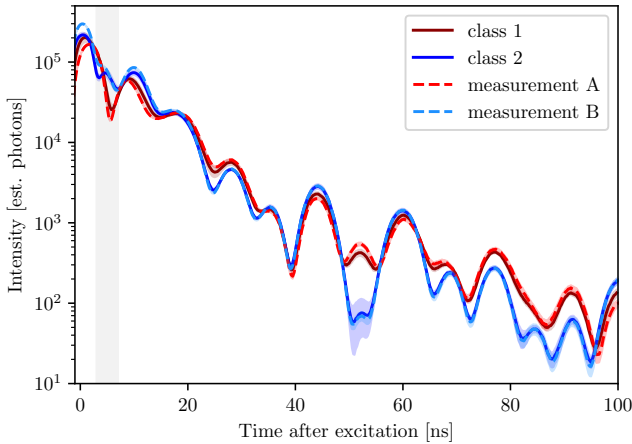


FIG. 4. Measured time-domain data in experimental settings A (red dashed) and B (blue dashed), which serve as a reference to benchmark the analysis. The 1σ uncertainty band of the measurements is indicated by the shaded area around the respective lines (see Appendix A). The corresponding results of the data-driven single-shot analysis (class 1 and 2) are shown as solid lines. Here an estimate of the uncertainty based on the data variability is given by the standard deviation of the subset analysis in Appendix F, which is drawn as the shaded band around the lines. The two time-domain datasets are scaled for better comparability by fitting an overall scaling factor from 0ns to 100ns. The ROI (3-7 ns) used for the analysis is indicated in gray.

tering quality and the optimum ROIs are similar over a broader range of N_{hs} , which indicates that the analysis is stable against variations in the analysis parameters.

After having identified the optimum analysis parameters based on the clustering quality \mathcal{S} , a further consistency check is possible by analyzing the individual silhouette scores s_i of the different shots in all clusters. Indeed, we find that our approach identified two clusters comparable in size, and that the majority of shots in both clusters has a high individual silhouette score (see Appendix E and Ext. Data Figure S5).

Once the dynamics classes are identified and corresponding models are generated, we proceed with the entire set of measured shots, independent of their signal content, and assign each shot to one of the models (see “sorting” in Fig. 2). Note that this comparison of individual shots with the generated models has a crucial advantage over the direct comparison of individual shots. A direct comparison of two shots with low signal content is subject to comparably high statistical uncertainties. In contrast, the statistical fluctuations are greatly reduced in the models comprising a number of shots, such that a comparison of a low-signal shot with one of the models is more reliable. For this comparison, we employ the negative Poissonian log-likelihood $P(a, b)$, regarding the individual shots as the data to be tested against the models. This sorting step results in one set of shots for each of the dynamics classes determined throughout the sorting.

The two sets of sorted data can now be analyzed individually. Summing over each set separately results in two time-dependent intensities, which reflect the nuclear dynamics in the two respective dynamics classes, and form the main results of the data-driven analysis. They are shown as solid lines in Fig. 4. The two time-dependent intensities clearly differ at certain times, e.g., around 5 ns and 50 ns as well as from 70 ns to 90 ns, indicating that the clustering algorithm indeed identified different types of dynamics. In order to verify the data-driven analysis approach, we finally unblind the information on the experimental settings for each of the shots, which we have due to the specific design of the underlying experiment, but which was not used during the data-driven analysis. The resulting “true” reference time-domain data for the two different dynamics classes are shown as dashed lines in Fig. 4. We find that the results of the data-driven analysis indeed follow the reference measurements closely. In particular, the regions with characteristic higher deviations between the two dynamics classes are well-reproduced in both cases. Interestingly, there are regions around 50ns, or after 70ns, are well-recovered even though they are far outside the analysis ROI from 3ns to 7ns used to generate the original models. Note that deviations at initial times up to 4ns are likely due to saturation effects (see Appendix B).

We have demonstrated the possibility to perform coherent nuclear forward scattering experiments using self-seeded XFEL radiation. The exceptionally high resonant flux per shot unlocks fundamentally new applications for Mössbauer nuclei. In particular, our results demonstrate the possibility to disentangle different evolution pathways from the out-of-equilibrium state back into equilibrium by analyzing time-domain datasets on the level of single shots. For this, we identify different dynamics classes and sort the data accordingly. Since the clustering analysis is data-driven and does not require a theoretical modeling of the data, also previously unknown phenomena can be searched for. The analysis can readily be applied to standard experimental approaches, without the need for dedicated measurements or instrumentation. Rather than analyzing each individual shot separately, our approach is to extract dynamics models from the data of the shots with the highest signal content. Subsequently, all shots can be sorted, i.e., assigned to one of the models. This way, also shots with lower signal-photon number can contribute to the analysis—even if their signal content is not sufficient for an individual analysis.

Importantly, we found that our sorting analysis is capable of clearly revealing the differences in the two dynamics classes also for times larger than approximately 50 ns after excitation. By contrast, even the rare shots with highest signal-photon number do not contain sufficient counts to resolve these differences in the dynamics directly, due to the overall approximately exponential decay of the scattered light intensity with time (see Appendix B). This highlights the advantage of the sorting approach over the direct single-shot analysis.

By repeating the clustering analysis for different final numbers of clusters, the most probable number of dynamics classes can be identified. In the present experiment, we find that an analysis with two clusters yields the highest clustering quality and stability, consistent with the original experimental design (see Appendix D). In practice, already a stable and reproducible identification of qualitatively different time-domain data is a clear indication that the experiment comprises different classes of dynamics (see Appendix F).

We envision that the single-shot sorting approach applied to coherent forward scattering data recorded with self-seeded x-ray pulses will open up new applications for Mössbauer science. Broadly speaking, different dynamics classes can originate from the nuclei themselves, or from the surrounding host environment. Under XFEL excitation conditions, even the unperturbed nuclear relaxation dynamics of a multiply-excited nuclear ensemble back to the ground state comprises different sequences of coherent and incoherent emission events. The time-resolved observation of the emitted photons can project the nuclear ensemble into entangled states [9], or correlate independent excitation volumes in the sample [7, 8]. An analysis on the single-shot level provides a route towards the observation of the nuclear ensemble in a quantum state. Furthermore, a major contribution to the incoherent decay is formed by internal conversion [49], such that our method provides an opportunity to study the interaction between the nuclei and the electronic environment in a controlled way. On the other hand, the majority of current-day applications of Mössbauer nuclei are related to studying the structure and dynamics of the surrounding host material. The host evolution may also impose different dynamics onto the nuclei, e.g., if it involves quantum-mechanical superposition states with probabilistic measurement outcomes. Our sorting approach opens an avenue to developing the nuclei as non-invasive high-resolution probes for the electronic, phononic and structural dynamics of the environment geared towards the unique excitation conditions at XFELs. At these machines, mostly interactions of the x-rays with electronic degrees of freedom are used to probe targets, while these electronic properties often-times are subject of the investigation themselves, such that the probe and the probed system are intrinsically intertwined. By contrast, nuclei form an independent subsystem, and thereby offer valuable complementary information. Key examples involve the dynamics after impulsive pumping of the electronic [13], vibrational [14], spin [15, 17] or magnetic [16] state of the host material. We further envision the extension of the sorting approach to nuclear inelastic scattering [14, 50], which next to the study of phonons could also allow one to generalize XFEL Mössbauer studies to liquids, gases, plasmas, higher-energy nuclear transitions, “detect-before-destruct” approaches, or other samples with low probability for recoilless x-ray-nucleus interactions [51, 52]. Furthermore, coherent control mechanisms with Mössbauer nuclei [12, 16]

could be transferred towards the single-shot domain.

Appendix A: Detection

Since the individual shots contain up to several hundred signal photons, the majority of which arrives in a comparably short time interval after the x-ray excitation, the employed APDs cannot distinguish the individual arriving photons. Therefore, rather than counting arrival times, we record the entire time-dependent voltage traces of the APDs using fast digitizers. As a result, the recorded time-domain data is convoluted by the detector response. For isolated signal photons, the detector response can be modeled using a Gaussian envelope of about 2.5 ns temporal full-width at half maximum. In order to estimate the uncertainty of the measurements, the recorded voltage traces are scaled with the area of the single-photon detector response, such that the area under the curve is equal to the estimated integrated number of photons. Subsequently, a Poissonian uncertainty can be applied.

Appendix B: Raw data

In Supplemental Fig. S1, the 20 shots with highest signal content are displayed. For comparison, the reference time-domain data obtained by averaging over all shots is displayed as the black dashed line. There are three important observations. First, up to 20 ns there is a strong deviation in the recorded intensity of the single shots as compared to the averaged time-domain data. This can be attributed to saturation effects in the detector, due to the limited dynamical range of the APDs employed in the experiment. This saturation is most pronounced at early times due to the overall approximately exponential decay of the scattered intensity with time. Furthermore, the saturation is strongest for the shots with highest signal content shown in the figure. By contrast, the majority of shots has a lower signal content, and therefore is less affected by the detector saturation. As a result, the averaged data deviates from the shots with highest signal content, and better represents the true amount of light scattered by the nuclei. Second, we can analyze whether the individual shots with highest signal content contain sufficient count statistics to allow for an analysis of the time-domain data on a single-shot basis. We find that this is indeed the case at short times, although bounded by the saturation effects discussed above. However, at times later than approximately 50 ns after the excitation, the recorded single-shot intensities approach the level of individual recorded photons, such that the dynamics can no longer be reconstructed reliably. Finally, we find that at times around 5 ns, the data of the subset of shots with highest signal content clearly divides into two different subsets. One exhibits a pronounced dip in the intensity, while the other subset remains approximately constant.

This feature is reflected by the region of interest from 3 ns to 7 ns identified by the clustering approach presented in the main text. Other features distinguishing the two dynamics classes A and B in our measurement are visible at later times in the averaged time-domain data, but they cannot be resolved on the single-shot level due to the low statistics. Around $t = 0$ ns, the averaged time-domain data comprise prompt scattering contributions, which can be attributed to the finite polarization extinction of the analyzer, the convolution of the signal with the single-photon detector response, and to background photons. Instead, the distinct feature at around 5 ns also appears in the corresponding idealized theory calculation, and can be attributed to the first quantum beat due to the interference of different scattering channels between the involved hyperfine states.

Appendix C: Signal content

Because the signal content should not be dominated by the high statistics at early times, but should account for a signal spread out over the entire analysis region, the signal content is defined by the area under the logarithm of the APD trace. A histogram of the distribution of signal content is displayed in Supplemental Fig. S2. In addition, in Supplemental Fig. S2 an estimate on the photon number corresponding to a certain range of signal content is given. To this end, 1000 single-shot traces with a specific photon number N are simulated by drawing N random numbers from the averaged time-domain data and summing up the single-photon detector response of those. For those artificial traces the signal content is calculated. To avoid influence of the saturation effects, the signal content is evaluated only after 20 ns. For each N this results in an approximately Gaussian distribution. Finally, for all shots in our measured dataset, whose signal content from 20 ns onwards lies within the 1σ interval around the mean of the Gaussian distribution, the mean and standard deviation of the signal content over the whole time range is calculated. This is the estimated signal content and its uncertainty for a given photon number N , which is indicated by the green dots and errorbars in the figure. It is important to note that the shots with highest signal content are statistical outliers, and the 20 spectra shown above only constitute a tiny fraction of the 362.610 shots measured during the experiment (181.350 shots for A, and 181.260 for B). To illustrate this further, example shots with high, medium and low signal content are shown in Supplemental Fig. S3. For the high signal content shots, the ten shots with highest signal content are used, for medium signal content the ten with highest signal content out of the lower half and for low signal content the ten highest out of the lowest 10%. The respective cutoffs are shown in Supplemental Fig. S2 as the dashed purple lines. In the high-signal single-shot data, the difference at around 5 ns is clearly visible while later features already lack statistics. In the shots with

medium signal content, the differences at around 5 ns are still partially visible, while the low signal shots contain only a small number of photons.

Appendix D: Sample and scattering geometries

The measurements were performed on a thin-film cavity fabricated by sputter deposition on a silicon substrate. The layer structure from bottom to top was determined as Si/Pt(14.8 nm)/ ^{57}Fe (15.3 nm)/Pt(2.1 nm), via fits to an electronic $\theta - 2\theta$ reflectivity curve measured at the P01 High Resolution Dynamics Beamline at the synchrotron radiation source PETRA III (at DESY in Hamburg) using the software packages GenX [53] and Nexus [54]. Using this structure, the incidence angles of the scattering geometry were then determined via fits to the time-dependent intensities measured at European XFEL using Nexus [54]. In these fits, the finite temporal width of the APD photon detection signals is modeled using a convolution with a Gaussian detector response. The theory fits together with the experimental data are shown in Supplemental Fig. S4. The incidence angles are obtained as 4.15 mrad and 4.03 mrad in the two measurements, respectively. These are close to the first minimum in the electronic reflection curve, corresponding to the resonant driving of the first cavity mode. Additionally, the two datasets feature a slightly different canting angle of the analyzer crystal, due to a realignment between the two measurements.

Appendix E: Silhouette score

The assessment of the clustering algorithm used in the main text is based on the overall clustering quality \mathcal{S} . As a more detailed consistency check for the clustering, the individual silhouette scores of the shots used for the model building are shown in Supplemental Fig. S5 for the optimum analysis parameters $N_{\text{hs}} = 20$ and analysis ROI between 3 ns and 7 ns. Each horizontal bar represents the silhouette score of a single shot with the colors indicating the cluster, to which the shot belongs. For better visibility, the clusters are spatially separated. A large fraction of the shots has a silhouette score larger than 0.5, many even larger than 0.8, indicating good clustering [55]. However, a few shots have a small silhouette score indicating that they do not so clearly belong to cluster. Nonetheless, those outliers are only few and together with the fact that a stable ROI is found, which is similar for different number of high-signal content shots N_{hs} , the model generation is reliable.

Appendix F: Stability of analysis

The stability, reproducibility and consistency of the analysis can be tested in various ways. First, one may

analyze the two time-domain datasets reconstructed from the data in the main text. To this end, we artificially create repetitions of the experiment with different statistical realizations of the photon detection by dividing the full dataset randomly into 5 subsets. Note that this division at the same time corresponds to a reduction of the effective measurement time realized in the experiment by a factor of 5, thereby rendering the analysis more challenging. Subsequently, the complete sorting algorithm described in the main part is applied to each of the subsets. To improve the statistics of this analysis, we repeat this procedure ten times with new randomly chosen subsets. Afterwards, the 50 reconstructed time-domain datasets can be compared to each other and their standard deviation at any instance in time provides an estimate of the uncertainty of the analysis due to data variability. For the sorting analysis discussed in the main part, the uncertainties are indicated as the shaded areas around the respective lines in Fig. 4. It can be seen that the uncertainties are small compared to the difference between the averaged time-domain data of the two measurement sets, such that they can reliably be distinguished.

Next, we can use a stability analysis in order to verify the identification of dynamics classes, as shown in Supplemental Fig. S6. As a first test, we perform the analysis only on the shots belonging to one of the measurements, A or B, while still enforcing the determination of two clusters in the clustering analysis. The results are shown in the left panel (a) of Supplemental Fig. S6. The red and blue solid lines display the recovered averaged time-domain data of the two classes. The dashed lines show the recovered time-domain data of Fig. 4 corresponding to class 1 (red dashed) and class 2 (blue dashed) as a reference. For better clarity, the two cases with data of measurement A and measurement B are shifted with respect to each other along the y axis. We find that

the two recovered datasets (test class 1 and test class 2) agree within their uncertainty, such that we conclude that the algorithm did not identify different dynamics classes. Furthermore, the recovered averaged time-domain datasets agree with the reference data for measurement A in case that the shots of A were used for the analysis, and analogously for B. Thus, the analysis works as expected.

In a third test, we repeat the analysis in the main text with data of both measurements A and B, but allow for three clusters in the clustering analysis. The corresponding results are shown in the right panel (b) of Supplemental Fig. S6. As a first observation, we find that the overall uncertainties are considerably larger than in the case with two clusters (see Fig. 4), indicating a less reliable analysis. Second, we find that two of the recovered time-domain data (test class 1 and test class 3) agree well with each other, within their respective uncertainties. They also agree well with the reference data “class 1” obtained with the analysis involving only two clusters in Fig. 4. Correspondingly, the third of the recovered time-domain data (test class 2) agrees well with the second reference data “class 2”. Thus, the analysis is consistent with only two dynamics classes in the data, as expected.

Overall, we therefore conclude that the sorting algorithm works as expected, in particular with regards to the correct number of dynamics classes extracted from the data.

ACKNOWLEDGMENTS

We acknowledge European XFEL in Schenefeld, Germany, for provision of X-ray free-electron laser beamtime at MID under proposal number 3334 and would like to thank the staff for their assistance, in particular W. Jo, J. Möller, A. Parenti and J. Wrigley.

[1] R. L. Mössbauer, Kernresonanzfluoreszenz von Gammastrahlung in Ir¹⁹¹, *Zeitschrift für Physik* **151**, 124 (1958).

[2] G. V. Smirnov, Coherent nuclear resonance fluorescence, in *The Rudolf Mössbauer Story: His Scientific Work and Its Impact on Science and History*, edited by G. Kalvius and P. Kienle (Springer, Berlin, Heidelberg, 2012).

[3] P. Gütlich, E. Bill, and A. X. Trautwein, *Mössbauer Spectroscopy and Transition Metal Chemistry: Fundamentals and Applications* (Springer Berlin, Heidelberg, 2011).

[4] E. Gerdau and H. de Waard (Ed.), Nuclear resonant scattering of synchrotron radiation, *Hyperfine Int.* 123-125 (1999/2000).

[5] J. B. Hastings, D. P. Siddons, U. van Bürck, R. Hollatz, and U. Bergmann, Mössbauer spectroscopy using synchrotron radiation, *Phys. Rev. Lett.* **66**, 770 (1991).

[6] G. K. Shenoy and R. Röhlsberger, Scientific opportunities in nuclear resonance spectroscopy from source-driven revolution, *Hyperfine Interactions* **182**, 157 (2008).

[7] C. Cabrillo, J. I. Cirac, P. García-Fernández, and P. Zoller, Creation of entangled states of distant atoms by interference, *Phys. Rev. A* **59**, 1025 (1999).

[8] D. L. Moehring, P. Maunz, S. Olmschenk, K. C. Younge, D. N. Matsukevich, L.-M. Duan, and C. Monroe, Entanglement of single-atom quantum bits at a distance, *Nature* **449**, 68 (2007).

[9] C. Thiel, J. von Zanthier, T. Bastin, E. Solano, and G. S. Agarwal, Generation of symmetric Dicke states of remote qubits with linear optics, *Phys. Rev. Lett.* **99**, 193602 (2007).

[10] G. Shenoy, Dreams with synchrotron radiation, in *The Rudolf Mössbauer Story: His Scientific Work and Its Impact on Science and History*, edited by G. Kalvius and P. Kienle (Springer, Berlin, Heidelberg, 2012).

[11] Y. V. Shvyd'ko, T. Hertrich, U. van Bürck, E. Gerdau, O. Leupold, J. Metge, H. D. Rüter, S. Schwendy, G. V. Smirnov, W. Potzel, and P. Schindelmann, Storage of nuclear excitation energy through magnetic switching, *Phys. Rev. Lett.* **77**, 3232 (1996).

[12] K. P. Heeg, A. Kaldun, C. Strohm, C. Ott, R. Subramanian, D. Lentrodt, J. Haber, H.-C. Wille, S. Goerttler, R. Rüffer, C. H. Keitel, R. Röhlsberger, T. Pfeifer, and J. Evers, Coherent x-ray-optical control of nuclear excitons, *Nature* **590**, 401 (2021).

[13] O. Kocharovskaya, R. Kolesov, and Y. Rostovtsev, Coherent optical control of Mössbauer spectra, *Phys. Rev. Lett.* **82**, 3593 (1999).

[14] F. G. Vagizov, E. K. Sadykov, and O. A. Kocharovskaya, Modulation of Mössbauer radiation by pulsed laser excitation, *JETP Letters* **96**, 812 (2013).

[15] S. Sakshath, K. Jenni, L. Scherthan, P. Würz, M. Herlitschke, I. Sergueev, C. Strohm, H.-C. Wille, R. Röhlsberger, J. Wolny, and V. Schünemann, Optical pump-nuclear resonance probe experiments on spin crossover complexes, *Hyperfine Interactions* **238**, 1 (2017).

[16] L. Bocklage, J. Gollwitzer, C. Strohm, C. F. Adolff, K. Schlage, I. Sergueev, O. Leupold, H.-C. Wille, G. Meier, and R. Röhlsberger, Coherent control of collective nuclear quantum states via transient magnons, *Science Advances* **7**, 10.1126/sciadv.abc3991 (2021).

[17] S. Sadashivaiah, J. A. Wolny, L. Scherthan, K. Jenni, A. Omlor, C. S. Müller, I. Sergueev, M. Herlitschke, O. Leupold, H.-C. Wille, R. Röhlsberger, and V. Schünemann, High-repetition rate optical pump–nuclear resonance probe experiments identify transient molecular vibrations after photoexcitation of a spin crossover material, *The Journal of Physical Chemistry Letters* **12**, 3240 (2021), pMID: 33764073, <https://doi.org/10.1021/acs.jpclett.0c03733>.

[18] V. Schünemann and H. Winkler, Structure and dynamics of biomolecules studied by Mössbauer spectroscopy, *Reports on Progress in Physics* **63**, 263 (2000).

[19] C. Krebs, J. C. Price, J. Baldwin, L. Saleh, M. T. Green, and J. M. Bollinger, Rapid freeze-quench ^{57}Fe Mössbauer spectroscopy: monitoring changes of an iron-containing active site during a biochemical reaction, *Inorganic chemistry* **44**, 742 (2005).

[20] W. Decking, S. Abeghyan, P. Abramian, A. Abramsky, A. Aguirre, C. Albrecht, P. Alou, M. Altarelli, P. Altmann, K. Amyan, *et al.*, A MHz-repetition-rate hard x-ray free-electron laser driven by a superconducting linear accelerator, *Nature photonics* **14**, 391 (2020).

[21] S. Liu, C. Grech, M. Guetg, S. Karabekyan, V. Kocharyan, N. Kujala, C. Lechner, T. Long, N. Mirian, W. Qin, S. Serkez, S. Tomin, J. Yan, S. Abeghyan, J. Anton, V. Blank, U. Boesenberg, F. Brinker, Y. Chen, W. Decking, X. Dong, S. Kearney, D. La Civita, A. Madsen, T. Maltezopoulos, A. Rodriguez-Fernandez, E. Saldin, L. Samoylova, M. Scholz, H. Sinn, V. Sleziona, D. Shu, T. Tanikawa, S. Terentiev, A. Trebushinin, T. Tschentscher, M. Vanonni, T. Wohlenberg, M. Yakopov, and G. Geloni, Cascaded hard x-ray self-seeded free-electron laser at megahertz repetition rate, *Nature Photonics* **17**, 984 (2023).

[22] P. Emma, R. Akre, J. Arthur, R. Bionta, C. Bostedt, J. Bozek, A. Brachmann, P. Bucksbaum, R. Cofee, F.-J. Decker, Y. Ding, D. Dowell, S. Edstrom, A. Fisher, J. Frisch, S. Gilevich, J. Hastings, G. Hays, P. Hering, Z. Huang, R. Iverson, H. Loos, M. Messerschmidt, A. Miahnahri, S. Moeller, H.-D. Nuhn, G. Pile, D. Ratner, J. Rzepiela, D. Schultz, T. Smith, P. Stefan, H. Tompkins, J. Turner, J. Welch, W. White, J. Wu, G. Yocky, and J. Galayda, First lasing and operation of an ångstrom-wavelength free-electron laser, *Nature Photonics* **4**, 641 (2010).

[23] W. Barletta, J. Bisognano, J. Corlett, P. Emma, Z. Huang, K.-J. Kim, R. Lindberg, J. Murphy, G. Neil, D. Nguyen, C. Pellegrini, R. Rimmer, F. Sannibale, G. Stupakov, R. Walker, and A. Zholents, Free electron lasers: Present status and future challenges, *Nuclear Instruments and Methods in Physics Research Section A: Accelerators, Spectrometers, Detectors and Associated Equipment* **618**, 69 (2010).

[24] T. Ishikawa, H. Aoyagi, T. Asaka, Y. Asano, N. Azumi, T. Bizen, H. Ego, K. Fukami, T. Fukui, Y. Furukawa, S. Goto, H. Hanaki, T. Hara, T. Hasegawa, T. Hattori, A. Higashiya, T. Hirono, N. Hosoda, M. Ishii, T. Inagaki, Y. Inubushi, T. Itoga, Y. Joti, M. Kago, T. Kameshima, H. Kimura, Y. Kirihara, A. Kiyomichi, T. Kobayashi, C. Kondo, T. Kudo, H. Maesaka, X. M. Maréchal, T. Masuda, S. Matsubara, T. Matsumoto, T. Matsushita, S. Matsui, M. Nagasono, N. Nariyama, H. Ohashi, T. Ohata, T. Ohshima, S. Ono, Y. Otake, C. Saji, T. Sakurai, T. Sato, K. Sawada, T. Seike, K. Shirasawa, T. Sugimoto, S. Suzuki, S. Takahashi, H. Takebe, K. Takeshita, K. Tamasaku, H. Tanaka, R. Tanaka, T. Tanaka, T. Togashi, K. Togawa, A. Tokuhisa, H. Tomizawa, K. Tono, S. Wu, M. Yabashi, M. Yamaga, A. Yamashita, K. Yanagida, C. Zhang, T. Shintake, H. Kitamura, and N. Kumagai, A compact x-ray free-electron laser emitting in the sub-ångström region, *Nature Photonics* **6**, 540 (2012).

[25] C. Bostedt, S. Boutet, D. M. Fritz, Z. Huang, H. J. Lee, H. T. Lemke, A. Robert, W. F. Schlotter, J. J. Turner, and G. J. Williams, Linac coherent light source: The first five years, *Rev. Mod. Phys.* **88**, 015007 (2016).

[26] J. Rossbach, J. R. Schneider, and W. Wurth, 10 years of pioneering x-ray science at the free-electron laser flash at desy, *Physics Reports* **808**, 1–74 (2019).

[27] J. Ullrich, A. Rudenko, and R. Moshammer, Free-electron lasers: New avenues in molecular physics and photochemistry, *Annual Review of Physical Chemistry* **63**, 635 (2012).

[28] A. I. Chumakov, A. Q. R. Baron, I. Sergueev, C. Strohm, O. Leupold, Y. Shvyd'ko, G. V. Smirnov, R. Rüffer, Y. Inubushi, M. Yabashi, K. Tono, T. Kudo, and T. Ishikawa, Superradiance of an ensemble of nuclei excited by a free electron laser, *Nature Physics* **14**, 261 (2018).

[29] J. Amann, W. Berg, V. Blank, F.-J. Decker, Y. Ding, P. Emma, Y. Feng, J. Frisch, D. Fritz, J. Hastings, *et al.*, Demonstration of self-seeding in a hard-x-ray free-electron laser, *Nature photonics* **6**, 693 (2012).

[30] I. Inoue, T. Osaka, T. Hara, T. Tanaka, T. Inagaki, T. Fukui, S. Goto, Y. Inubushi, H. Kimura, R. Kinjo, H. Ohashi, K. Togawa, K. Tono, M. Yamaga, H. Tanaka, T. Ishikawa, and M. Yabashi, Generation of narrow-band x-ray free-electron laser via reflection self-seeding, *Nature photonics* **13**, 319 (2019).

[31] I. Nam, C.-K. Min, B. Oh, G. Kim, D. Na, Y. J. Suh, H. Yang, M. H. Cho, C. Kim, M.-J. Kim, C. H. Shim, J. H. Ko, H. Heo, J. Park, J. Kim, S. Park, G. Park, S. Kim, S. H. Chun, H. Hyun, J. H. Lee, K. S. Kim, I. Eom, S. Rah, D. Shu, K.-J. Kim, S. Terentyev, V. Blank, Y. Shvyd'ko, S. J. Lee, and H.-S. Kang, High-brightness self-seeded x-ray free-electron laser covering

the 3.5 keV to 14.6 keV range, *Nature Photonics* **15**, 435 (2021).

[32] Y. Shvyd'ko, R. Röhlsberger, O. Kocharovskaya, J. Evers, G. A. Geloni, P. Liu, D. Shu, A. Miceli, B. Stone, W. Hippler, B. Marx-Glowna, I. Uschmann, R. Loetzscher, O. Leupold, H.-C. Wille, I. Sergeev, M. Gerharz, X. Zhang, C. Grech, M. Guetg, V. Kocharyan, N. Kujala, S. Liu, W. Qin, A. Zozulya, J. Hallmann, U. Boesenberg, W. Jo, J. Möller, A. Rodriguez-Fernandez, M. Youssef, A. Madsen, and T. Kolodziej, Resonant x-ray excitation of the nuclear clock isomer ^{45}Sc , *Nature* **622**, 471 (2023).

[33] O. Y. Gorobtsov, G. Mercurio, F. Capotondi, P. Skopintsev, S. Lazarev, I. A. Zaluzhnyy, M. B. Danailov, M. Dell'Angela, M. Manfredda, E. Pedersoli, L. Giannessi, M. Kiskinova, K. C. Prince, W. Wurth, and I. A. Vartanyants, Seeded x-ray free-electron laser generating radiation with laser statistical properties, *Nature communications* **9**, 4498 (2018).

[34] R. Neutze, R. Wouts, D. van der Spoel, E. Weckert, and J. Hajdu, Potential for biomolecular imaging with femtosecond x-ray pulses, *Nature* **406**, 752 (2000).

[35] J. C. H. Spence, U. Weierstall, and H. N. Chapman, X-ray lasers for structural and dynamic biology, *Reports on Progress in Physics* **75**, 102601 (2012).

[36] I. Schlichting, Serial femtosecond crystallography: the first five years, *IUCrJ* **2**, 246 (2015).

[37] S. Dold, T. Reichenbach, A. Colombo, J. Jordan, I. Barke, P. Behrens, N. Bernhardt, J. Correa, S. Düsterer, B. Erk, T. Fennel, L. Hecht, A. Heilrath, R. Irsig, N. Iwe, P. Kolb, B. Kruse, B. Langbehn, B. Manschwetus, P. Marienhagen, F. Martinez, K.-H. Meiweis-Broer, K. Oldenburg, C. Passow, C. Peltz, M. Sauppe, F. Seel, R. M. P. Tanyag, R. Treusch, A. Ulmer, S. Walz, M. Moseler, T. Möller, D. Rupp, and B. von Issendorff, Melting, bubblelike expansion, and explosion of superheated plasmonic nanoparticles, *Physical Review Letters* **134**, 10.1103/physrevlett.134.136101 (2025).

[38] J. Zimmermann, F. Beguet, D. Guthruf, B. Langbehn, and D. Rupp, Finding the semantic similarity in single-particle diffraction images using self-supervised contrastive projection learning, *npj Computational Materials* **9**, 10.1038/s41524-023-00966-0 (2023).

[39] C. Klose, F. Büttner, W. Hu, C. Mazzoli, K. Litzius, R. Battistelli, S. Zayko, I. Lemesh, J. M. Bartell, M. Huang, C. M. Günther, M. Schneider, A. Barbour, S. B. Wilkins, G. S. D. Beach, S. Eisebitt, and B. Pfau, Coherent correlation imaging for resolving fluctuating states of matter, *Nature* **614**, 256–261 (2023).

[40] M. Harmand, R. Coffee, M. R. Bionta, M. Chollet, D. French, D. Zhu, D. Fritz, H. Lemke, N. Medvedev, B. Ziaja, S. Toleikis, and M. Cammarata, Achieving few-femtosecond time-sorting at hard x-ray free-electron lasers, *Nature Photonics* **7**, 215 (2013).

[41] N. Hartmann, G. Hartmann, R. Heider, M. S. Wagner, M. Ilchen, J. Buck, A. O. Lindahl, C. Benko, J. Grünert, J. Krzywinski, J. Liu, A. A. Lutman, A. Marinelli, T. Maxwell, A. A. Miahnahri, S. P. Moeller, M. Planas, J. Robinson, A. K. Kazansky, N. M. Kabachnik, J. Viehhaus, T. Feurer, R. Kienberger, R. N. Coffee, and W. Helml, Attosecond time-energy structure of x-ray free-electron laser pulses, *Nature Photonics* **12**, 215–220 (2018).

[42] L. Funke, M. Ilchen, K. Dingel, T. Mazza, T. Mullins, T. Otto, D. E. Rivas, S. Savio, S. Serkez, P. Walter, N. Wieland, L. Wülfing, S. Bari, R. Boll, M. Braune, F. Calegari, A. D. Fanis, W. Decking, A. Duensing, S. Düsterer, F. Egun, A. Ehresmann, B. Erk, D. E. F. de Lima, A. Galler, G. Geloni, J. Grünert, M. Guetg, P. Grychtol, A. Hans, A. Held, R. Hindriksson, T. Jahnke, J. Laksman, M. Larsson, J. Liu, J. P. Marangos, L. Marder, D. Meier, M. Meyer, N. Mirian, C. Ott, C. Passow, T. Pfeifer, P. Rupprecht, A. Schletter, P. Schmidt, F. Scholz, S. Schott, E. Schneidmiller, B. Sick, K. Tiedtke, S. Usenko, V. Wanie, M. Wurzer, M. Yurkov, V. Zhaunerchyk, and W. Helml, Capturing nonlinear electron dynamics with fully characterised attosecond x-ray pulses, arXiv:2408.03858 [physics.optics] (2024).

[43] M. Straub, T. Ding, M. Rebholz, G. D. Borisova, A. Magunia, H. Lindenblatt, S. Meister, F. Trost, Y. Wang, S. Palutke, M. Braune, S. Düsterer, R. Treusch, C. H. Greene, R. Moshammer, T. Pfeifer, and C. Ott, Differential measurement of electron ejection after two-photon two-electron excitation of helium, *Phys. Rev. Lett.* **129**, 183204 (2022).

[44] A. Madsen, J. Hallmann, G. Ansaldi, T. Roth, W. Lu, C. Kim, U. Boesenberg, A. Zozulya, J. Möller, R. Shayduk, M. Scholz, A. Bartmann, A. Schmidt, I. Lobato, K. Sukharnikov, M. Reiser, K. Kazarian, and I. Petrov, Materials imaging and dynamics (MID) instrument at the European x-ray free-electron laser facility, *Synchrotron Radiation* **28**, 637 (2021).

[45] W. L. Bond, Precision lattice constant determination, *Acta Crystallographica* **13**, 814 (1960).

[46] J. H. Ward Jr, Hierarchical grouping to optimize an objective function, *Journal of the American statistical association* **58**, 236 (1963).

[47] S. C. Johnson, Hierarchical clustering schemes, *Psychometrika* **32**, 241 (1967).

[48] P. J. Rousseeuw, Silhouettes: a graphical aid to the interpretation and validation of cluster analysis, *Journal of computational and applied mathematics* **20**, 53 (1987).

[49] W. D. Loveland, D. J. Morrissey, and G. T. Seaborg, *Modern Nuclear Chemistry* (John Wiley & Sons, Ltd, 2017).

[50] A. Chumakov and R. Rüffer, Nuclear inelastic scattering, *Hyperfine Interactions* **113**, 59 (1998).

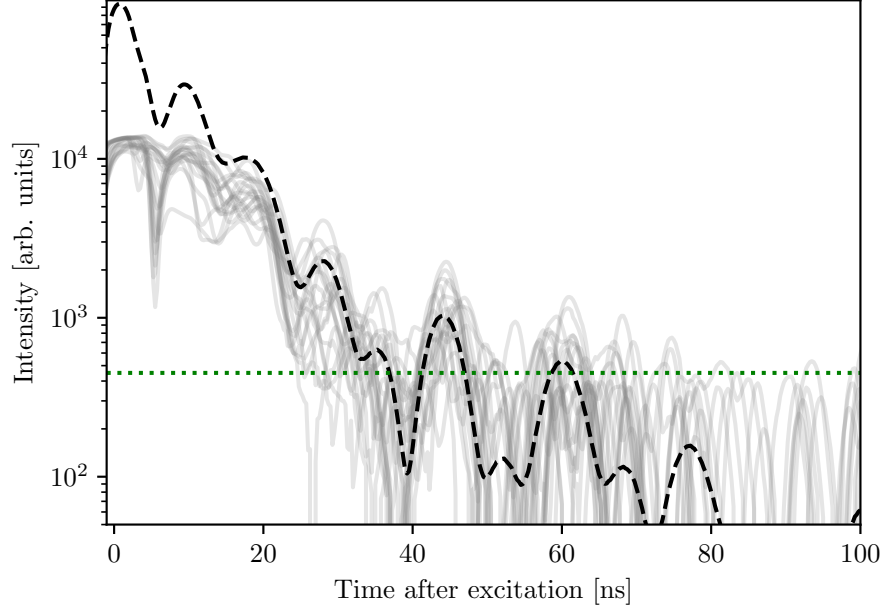
[51] A. Q. R. Baron, A. I. Chumakov, R. Rüffer, H. Grünsteudel, H. F. Grünsteudel, and O. Leupold, Single-nucleus quantum beats excited by synchrotron radiation, *Europhysics Letters* **34**, 331 (1996).

[52] I. Sergueev, U. van Bürck, A. I. Chumakov, T. Asthalter, G. V. Smirnov, H. Franz, R. Rüffer, and W. Petry, Synchrotron-radiation-based perturbed angular correlations used in the investigation of rotational dynamics in soft matter, *Phys. Rev. B* **73**, 024203 (2006).

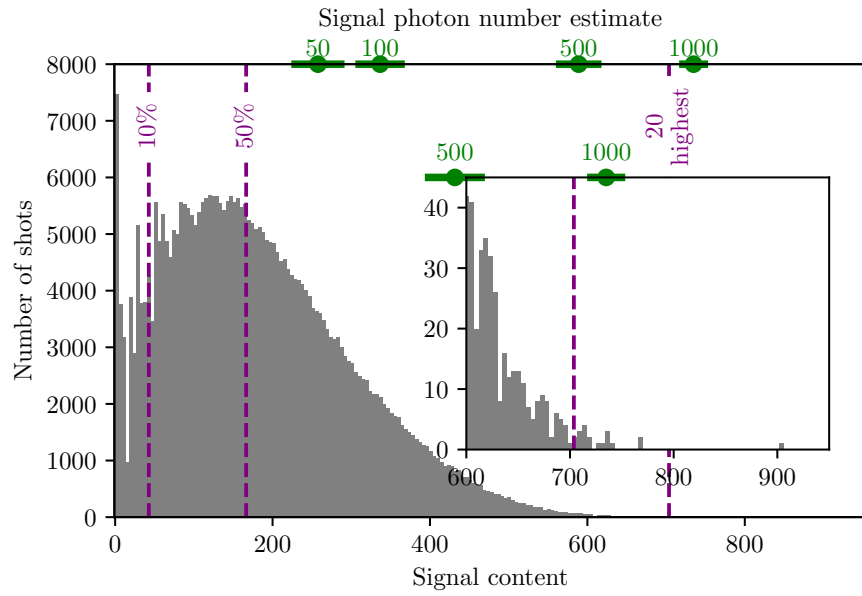
[53] A. Glavic and M. Björck, *GenX 3*: the latest generation of an established tool, *Journal of Applied Crystallography* **55**, 1063 (2022).

[54] L. Bocklage, Nexus - nuclear elastic x-ray scattering universal software, Zenodo, <https://zenodo.org/doi/10.5281/zenodo.7716207> (2024).

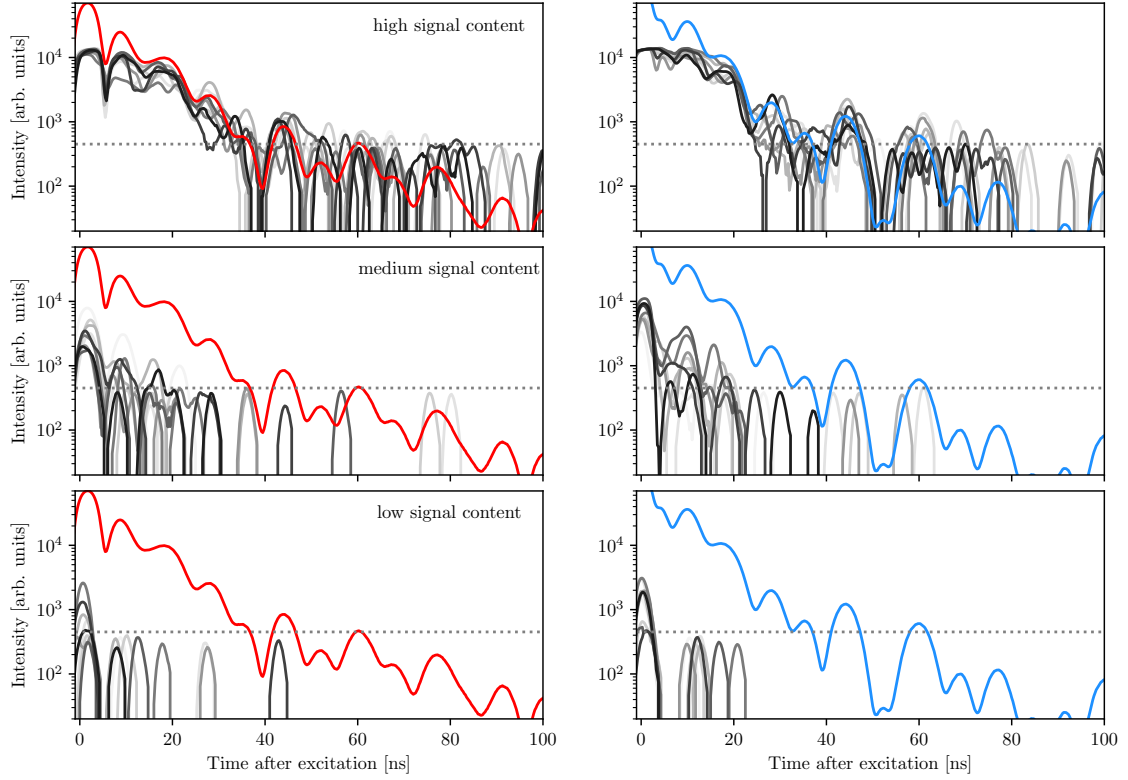
[55] L. Kaufman and P. J. Rousseeuw, *Finding groups in data: an introduction to cluster analysis* (John Wiley & Sons, 2005).



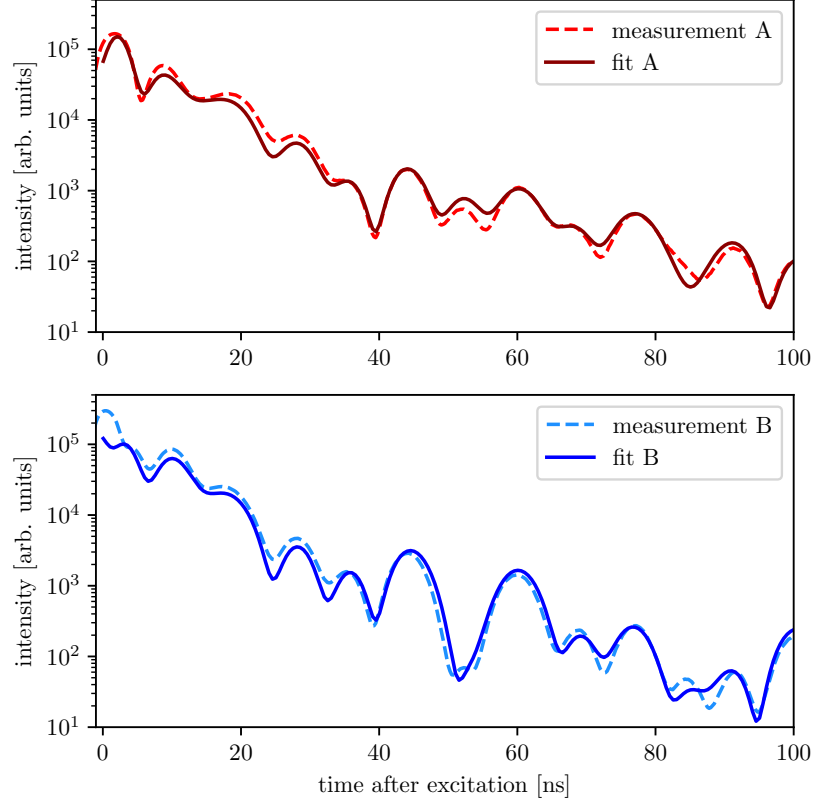
Supplemental Fig. S1. Example high-signal shots. Out of the full dataset, the 20 shots with highest signal content are shown in gray. The lines are plotted semi-transparent. This way, for example, the individual single-photon detection events at late times can be distinguished from the overlapping data at early times via the plot density. The black dashed line displays the time-domain data averaged over the full dataset. The green dotted line indicates the average height of the APD signal for individual recorded photons.



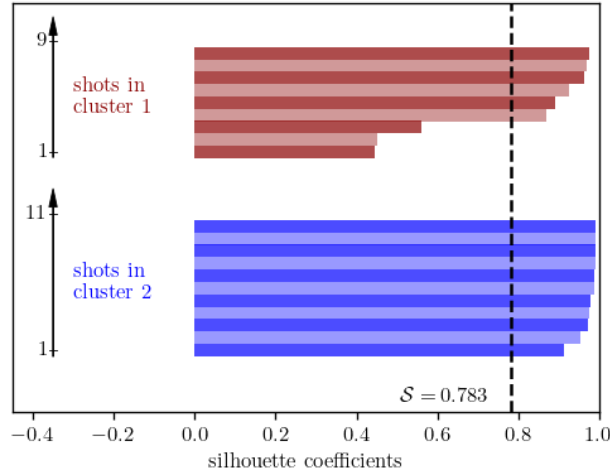
Supplemental Fig. S2. Histogram of the signal content. A histogram of the signal content in the single shots. Estimates on the corresponding photon numbers and their uncertainties are indicated by the green bars on the top axis. For details on the photon number estimate Appendix C. In addition, the purple dashed lines indicate low (10% of the traces), medium (50% of the traces) and high (20 highest traces) signal content as used in Supplemental Fig. S3. The inset shows a zoom into the highest signal region.



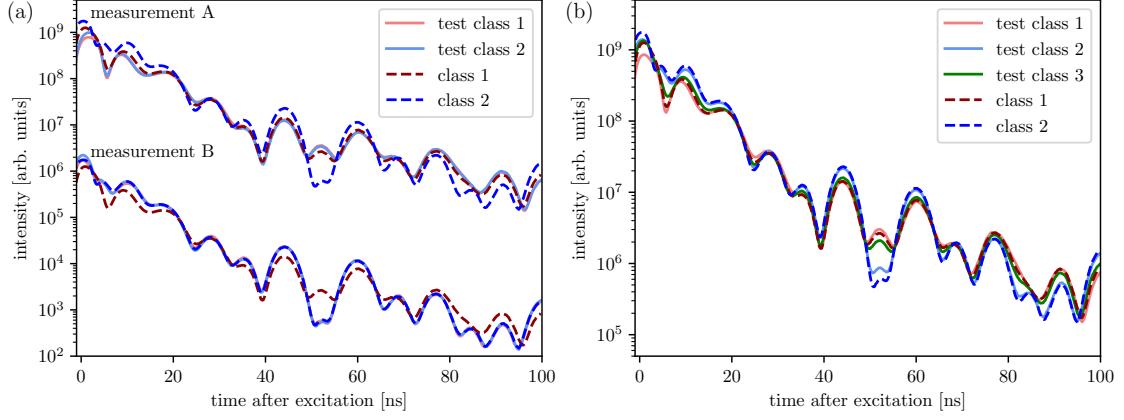
Supplemental Fig. S3. Example single-shot time-domain data. For measurement A (left column) and B (right), ten single-shot examples with high (top row), medium (center) and low (bottom) signal content, respectively, are shown in different shades of gray. The selected traces are the ones with highest signal content overall (high), of the lower half of the shots according to the signal content (medium) and of the lowest 10% of the shots according to the signal content (low). In red (blue) the averaged data belonging to measurement A (B) are displayed. The gray dashed line indicates the average height of the APD signal for individual recorded photons.



Supplemental Fig. S4. Raw data of the two measurements with theory fits. The upper panel shows an average over all shots of dataset A, the lower one the corresponding results of dataset B. In both panels, the dashed line shows the experimental measurement, while the solid line shows the corresponding theory fit. Details are given in Appendix D.



Supplemental Fig. S5. Individual silhouette coefficients for the shots used in the model building. The figure shows the individual silhouette scores of the $N_{hs} = 20$ shots of the experiment used for the model-building. The ROI for comparing different shots ranges from 3 ns to 7 ns. Each bar represents one shot with the colors indicating to which cluster the respective shot belongs. There are 9 shots in cluster 1, and 11 in cluster 2. The mean clustering quality $S = 0.783$ is represented by the dashed black line.



Supplemental Fig. S6. Stability of analysis. (a) In the top part of the panel, the analysis is only performed on the shots from measurement A. The lines "test class 1/2" show the time-domain data of the two reconstructed classes. For comparison, the dashed lines ("class 1" and "class 2") represent the analysis results of the full dataset from the main text in Fig. 4. It can be seen that for the dataset restricted to measurement A, the two recovered classes agree with each other within their uncertainty, as expected. Furthermore, they agree well with "class 1", which corresponds to measurement A. For completeness, the same analysis is performed with the data only from measurement B and shown in the lower part of the panel. For better visibility, the results for data for the two measurement settings are shifted along the y-axis such that they can be better distinguished from each other. (b) Results of the sorting analysis applied to the full dataset comprising measurement settings A and B, but with clustering into three classes. The results of these three test classes are shown as solid lines. The time-domain data is scaled for better comparability by fitting an overall scaling factor in the time range from 0ns to 100ns. The uncertainty bands of the different sets are calculated by a statistical analysis as explained in Appendix F. As a reference, also the results of the sorting analysis from the main text in Fig. 4 are displayed in addition (dashed lines "class 1" and "class 2").